Appl. Phys. B 85, 185–197 (2006)
DOI: 10.1007/s00340-006-2281-3

Applied Physics B
Lasers and Optics

Application of a difference-frequency-mixing based diode-laser sensor for carbon monoxide detection in the 4.4–4.8 μm spectral region

R. BARRON-JIMENEZ[1]
J.A. CATON[1]
T.N. ANDERSON[2]
R.P. LUCHT[2,✉]
T. WALTHER[3]
S. ROY[4]
M.S. BROWN[4]
J.R. GORD[5]

[1] Department of Mechanical Engineering, Texas A&M University, College Station, TX 77843-3123, USA
[2] School of Mechanical Engineering, Purdue University, West Lafayette, IN 47907-2088, USA
[3] Institute for Applied Physics, TU Darmstadt, Schlossgartenstr. 7, 64289 Darmstadt, Germany
[4] Innovative Scientific Solutions, Inc., 2766 Indian Ripple Rd., Dayton, OH 45440-3638, USA
[5] Air Force Research Laboratory, Propulsion Directorate, Wright-Patterson Air Force Base, OH 45433-7251, USA

Received: 16 November 2005/Revised version: 20 April 2006

ABSTRACT An all-solid-state continuous-wave (cw) laser system for mid-infrared absorption measurements of the carbon monoxide (CO) molecule has been developed and demonstrated. The single-mode, tunable output of an external-cavity diode laser (ECDL) is difference-frequency mixed with the output of a 550-mW diode-pumped cw Nd:YAG laser in a periodically poled lithium niobate (PPLN) crystal to generate tunable cw radiation in the mid-infrared region. The wavelength of the 860-nm ECDL can be coarse tuned from 860.782 to 872.826 nm, allowing the sensor to be operated in the spectral region 4.4–4.8 μm. CO-concentration measurements were performed in $CO/CO_2/N_2$ mixtures in a room-temperature gas cell, in the exhaust stream of a well-stirred reactor (WSR) at Wright-Patterson Air Force Base and in a near-adiabatic hydrogen/air CO_2-doped flame. The noise equivalent detection limits were estimated to be 1.1 and 2.5 ppm per meter for the gas cell and flame experiments, respectively. These limits were computed for combustion gas at 1000 K and atmospheric pressure assuming a signal-to-noise ratio of 1. The sensor uncertainty was estimated to be 2% for the gas-cell measurements and 10% for the flame measurements based on the repeatability of the peak absorption.

PACS 07.07.Df; 42.62.Fi; 42.65.Ky; 42.72.Ai

1 Introduction

Increasing concern over the environmental impact of combustion emissions has brought many new governmental regulations in recent years. In response to these restrictions, manufacturers are producing new equipment capable of extremely low levels of pollutant emissions. Currently, advanced power-generating gas turbines emit less than 10 ppm of nitric oxide (NO) and carbon monoxide (CO). These emission levels lie near the lowest detection limit of the current sensor technology.

Diode-laser-based absorption sensors are non-intrusive, and they offer high sensitivity and the potential for combustion control through real-time measurements of trace species. Several groups have been pursuing research for the detection of CO using tunable infrared diode-laser spectroscopy. Mihalcea et al. [1, 2] developed a diode-laser-based absorption system capable of CO detection using a tunable external-cavity InGaAsP diode laser in the spectral range 1.49–1.58 μm. The CO transitions in the second overtone band (1.3–2 μm region) are four orders of magnitude weaker than those in the fundamental band. Furthermore, the spectral interference from major species such as carbon dioxide (CO_2) and water (H_2O) are very strong in this spectral region, making it difficult to extract quantitative concentration of CO from the experimental spectrum. Several groups [3, 4] have also taken advantage of the CO_2 and H_2O interferences to perform multi-species detection using a similar laser system.

Transition lines in the first-overtone band of CO are one to two orders of magnitude stronger than those in the second-overtone band, and several transitions in the R branch are isolated from spectral interferences from CO_2 and H_2O. Wang et al. [5, 6] performed absorption measurements on the first-overtone band of the CO molecule using room-temperature, continuous-wave (cw), single mode InGaAsSb/AlGaAsSb diode lasers operated near 2.3 μm in an atmospheric pressure ethylene/air flame. The concentrations of CO were determined by interrogating two transitions in the first-overtone region. The $R(30)$ CO transition at 4343.81 cm^{-1} was used for measurements in the post-flame region (1.5 cm above the burner surface). The $R(15)$ CO transition at 4311.96 cm^{-1} was used for measurements in the exhaust duct (120-cm-long duct located 79 cm from the burner surface). For measurements in the post-flame zone, CO concentrations in rich flames were in good agreement with the chemical-equilibrium predictions. For direct-absorption measurements in the exhaust, a detection limit of 1.5 ppm-m at 470 K was demonstrated for a measurement time of 0.1 s with a detection bandwidth of 50 kHz. By using wavelength-modulation-spectroscopy techniques, system sensitivity of 0.1 ppm-m was achieved for a total measurement time of 0.4 s and a detection bandwidth of 500 Hz. For some years after this study, no DFB diode lasers were available near 2.3 μm. Currently, distributed feedback (DFB) diode lasers near 2.3 μm are commercially available [7, 8]. Ebert et al. [9] have used this new generation DFB lasers to interrogate the $R(30)$ CO transition. They performed direct-absorption measurements of CO con-

---

✉ Fax: (765) 494-0539, E-mail: lucht@ecn.purdue.edu

centrations in the post-combustion chamber of a hazardous waste incinerator achieving a detection limit of 6.5 ppm for a 1.0 s measurement time through a 2.5 m optical path length.

To access the fundamental band (near 4.6 μm) of carbon monoxide, lead-salt diode-lasers are available and have been extensively used [10–14]. Although successful in detecting CO, the use of in situ sensors based on lead-salt diodes has been limited due to operational complexity, the requirement of cryogenic cooling of the lasers, and multimode operation of the laser system. The recent development of quantum-cascade distributed-feedback (QC-DFB) lasers has allowed spectroscopic monitoring of CO in ambient air and flames [15, 16]; however, cw non-cryogenic versions of these systems are still not available.

A second strategy to obtain mid-infrared radiation is by nonlinear optical parametric frequency conversion; this strategy offers broad tunability, narrow linewidth, broadband parametric gain, efficient continuous-wave (cw) single-pass conversion, near-room-temperature operation, and the use of many mature laser technologies to seed the nonlinear conversion to IR [17]. Several groups have reported spectroscopic measurements of H_2O, CO_2, CO, NO, C_2H_2, C_6H_6, CH_4, C_2H_4, OCS [18], and other molecules in the IR region using difference-frequency-mixing (DFM) sources. Schade et al. [19] used a $AgGaS_2$ crystal to obtain DFM radiation in resonance with line $P(28)$ in the fundamental band of CO at 2022.914 cm^{-1}. In a similar but modular set up, Kelz et al. [20] used the same birefringent nonlinear crystal, $AgGaS_2$, to address the spectral region around 4.76 μm. These systems produced low levels of mid-IR radiation from moderate power diode lasers. Schade et al. used 30- and 50-mW input beams to produce 200 nW, while Keltz et al. typically produced >100 nW of mid-IR radiation from 20- and 6-mW beams.

Quasi-phase-matched (QPM) materials have many advantages for the production of mid-infrared radiation through nonlinear conversion. QPM materials (e.g., $LiNbO_3$, $LiTaO_3$, $KTiOPO_4$, $RbTiOAsO_4$) can be engineered to use the largest nonlinear susceptibility component of the material. The power-conversion efficiency of DFM processes in QPM periodically poled lithium niobate (PPLN) is typically one order of magnitude higher than the conversion efficiency in birefringent materials [18].

Absorption sensors based on the use of a PPLN crystal to produce mid-infrared radiation in a DFM process have been applied for the detection of trace gases [21–23]. Petrov et al. [24] investigated the feasibility of applying of a diode-pumped mid-IR difference-frequency-mixing (DFM) source based on a periodically poled $LiNbO_3$ (PPLN) crystal to detect atmospheric CO, N_2O, and CO_2. Their tunable mid-IR DFM source mixed a diode-pumped Nd:YAG ring laser (220 mW at 1064 nm) and 820 mW from a high power GaAlAs tapered amplifier seeded at 860 nm by a diode laser that allows for fast-frequency tuning by means of current modulation. A maximum of 8 μW were measured at 4.5 μm; however, CO-concentration measurements were typically performed with 3 μW of mid-IR power. With this system Petrov et al. accessed the CO fundamental band at the $R(6)$ transition near 2169 cm^{-1}. The detection sensitivity of $5\ \mathrm{ppb-m}/\sqrt{\mathrm{Hz}}$ was extrapolated based on rms noise measured in the $2f$ spectra under interference-free conditions in the 4.31–4.63 μm spectral region.

The system described here is based on the DFM of two near-infrared solid-state lasers in a PPLN crystal to produce tunable laser radiation in the 4.2–4.8 μm spectral region. The sensor system takes advantage of a new, compact diode-pumped Nd:YAG laser system and the incorporation of an external-cavity diode laser (ECDL) that allows for frequency tuning. The application of this sensor to mid-infrared, single-pass direct optical absorption measurements of the CO molecule is discussed in this paper. Preliminary CO-concentration measurements have been previously reported in laboratory and real combustion conditions [25] including an operating gas turbine [26]. Three experiments are discussed here. These are: (1) $CO/CO_2/N_2$ mixtures in a room-temperature gas cell, (2) in the exhaust of a well-stirred reactor (WSR), and (3) in a near-adiabatic hydrogen/air CO_2-doped flame. Spectral interferences were investigated in detail in the CO_2-doped flame measurements, and CO spectral lines with minimal CO_2 and H_2O absorption interferences were identified. The simplicity and relatively low cost of the DFM-based sensor described here make it an attractive system that is potentially applicable to numerous other interesting molecules in the infrared spectral region.

2 Experimental system and procedure

2.1 CO-*sensor system*

The schematic diagram of the experimental system is shown in Fig. 1. The mid-IR sensor system is based on DFM of the laser radiation from a 1064-nm, diode-pumped, 500-mW Nd:YAG laser system (IRCL-1064-500-S from CrystaLaser LC) and a tunable, 860-nm ECDL (DL-100 from Toptica Photonics AG) in a periodically poled lithium niobate (PPLN) crystal (Deltronic Crystal Industries Inc.). The PPLN crystal is 40 mm long, 0.5 mm thick, and has a quasi-phase-match period of 22.8 μm.

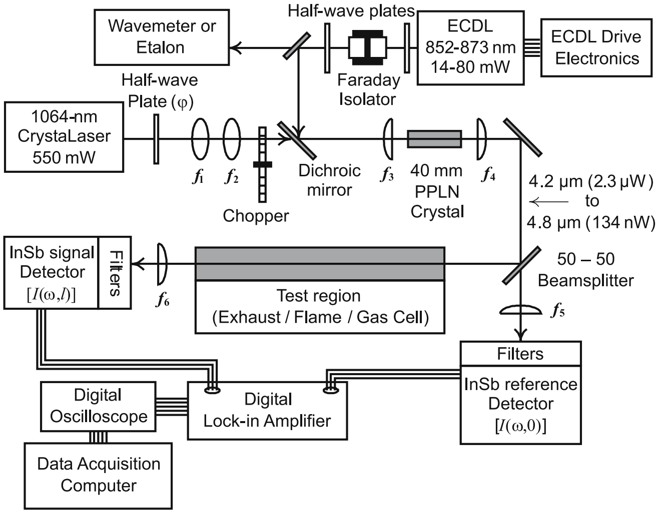

FIGURE 1 Experimental system for the CO-absorption measurements. $f_1 = +25.4$ mm, $f_2 = +50.2$ mm, $f_3 = +300$ mm, $f_4 = +150$ mm, $f_5 = +200$ mm, and $f_6 = +150$ mm

The vacuum wavelength of the 1064-nm Nd:YAG laser was measured to be 1064.664 nm using a Burleigh WA-1000 cw wavemeter. The major advantages of the diode-pumped Nd:YAG system are its excellent beam quality (TEM_{00}), narrow bandwidth (< 10 kHz), stability ($< 2\%$ over 24 h), compactness ($3 \times 3 \times 12$ cm), operability (no special cooling required), and reliability. The wavelength of the ECDL system can be tuned coarsely so that the DFM output beam can be tuned into resonance with various CO transitions in the fundamental band. The bandwidth of the ECDL output radiation was specified by the manufacturer to be ~ 1 MHz. The frequency spectrum of the ECDL was constantly monitored with a Burleigh SA Plus spectrum analyzer (2-GHz free spectral range) as the ECDL output was scanned, typically, over a mode-hop-free tuning range of 12 GHz. The use of a 36-dB Faraday isolator was required to block the back reflections into the ECDL and ensure single-mode operation. With the use of the isolator, no spectral jitter was observed while tuning the ECDL laser.

Several factors were considered to optimize the DFM conversion in the PPLN crystal. Both fundamental beams were carefully overlapped on a dichroic mirror and then focused using a plano-convex 300-mm-focal-length lens in the middle of the PPLN crystal. With this lens, the Rayleigh ranges of the fundamental beams were approximately 17 mm, which is approximately equal to one-half of the length of the PPLN crystal. The waist diameters of the beams were just small enough to be contained within the crystal body. To correct for the different focusing characteristics of the 860-nm and 1064-nm beams, a telescope was used in the 1064-nm beam path to adjust the 1064-nm beam waist position and size. The telescope consisted of two bi-convex lenses with focal lengths of $+25.4$ mm and $+50.2$ mm.

An alignment procedure was developed to ensure proper spatial overlap of the fundamental beams in the crystal. A visible HeNe laser included in the optical path of the 1064-nm beam was used to facilitate the alignment of the sensor. For coarse alignment, two apertures were placed before and after the PPLN crystal. Both input beams were directed through the center of these apertures. Two mirrors in the optical path for each input beam provided enough degrees of freedom to align the lasers through these apertures. Thus, the 860-nm and 1064-nm beams were roughly collinear and focused close to the same axial location. A 150-µm-diameter pinhole was then used to perform more precise alignment of the beams. Since the waist of the input beams was larger than the pinhole diameter, the beam was partially blocked. Maximum power transmission through the pinhole indicated the position of the center of the beam in the radial direction. By comparing the peak transmitted power measurements at different axial locations, we found the beam waist. The waist of the 860-nm beam was determined by the beam diameter and the $f = +300$ mm focusing lens; the waist location of this beam was fixed for a specific ECDL wavelength setting. The axial location of the 1064-nm beam waist was then determined. The spacing of the lenses in the 1064-nm telescope was then adjusted so that the location of the 1064-nm beam waist coincided with the axial location of the 860-nm beam waist. The collinearity of the 1064-nm and 860-nm beams was then checked by using the pinhole in the positions 12.5 mm before and after the waist location. Typically the paths of the 860-nm beam and HeNe laser were adjusted to match the path of the 1064-nm beam. Next, the PPLN crystal was placed in the system with its center at the axial location of the waist of the input beams. The oven that housed the PPLN crystal was mounted on a kinematic mount with five degrees of freedom to allow precise orientation of the PPLN crystal. The constant-temperature oven allowed adjustment of the longitudinal spatial period of the crystal structure to optimize the DFM process for a particular combination of fundamental frequencies. The polarizations of the 1064-nm and 860-nm beams were also adjusted to optimize DFM in the PPLN crystal. Half-wave plates were located in the beam paths upstream of the dichroic mirror to allow adjustment of the polarization of each beam. The 1064-nm Nd:YAG laser power was measured to be 570 mW. However due to the polarization characteristics of the dichroic mirror and the DFM process, the polarization was adjusted to maximize the DFM efficiency, thus sacrificing some power in the transmission through the dichroic mirror. The actual 1064-nm power measured in front of the PPLN entrance face was 320 mW. Similarly, some ECDL power was lost in the reflection from the dichroic mirror because the polarization was adjusted to maximize the DFM efficiency. The power values for the ECDL listed in Table 1 were measured just in front of the PPLN crystal.

The mid-infrared radiation generated in the PPLN crystal was collimated using a plano-convex calcium fluoride (CaF_2) lens ($f = +150$ mm) after exiting the PPLN crystal. The mid-infrared beam was then split into a “signal” beam and a “reference” beam using a 50-50 beamsplitter. The signal beam was directed through the “test region”. In this paper three “test regions” are discussed: i) a gas cell filled with a mixture of CO and other buffer gases, ii) the exhaust of a well-stirred reactor (WSR), and iii) the post-flame region of a hydrogen/air flame doped with CO_2. The signal beam was focused using a plano-convex CaF_2 lens with a focal length of 150 mm onto a cryogenically cooled InSb detector after passing through a long-wave-pass filter. The reference beam was focused using a plano-convex CaF_2 lens with a focal length of 200 mm onto a second InSb detector, again after being transmitted through a long-wave-pass filter. The filter, with cut off at 3.5 µm, rejected the 860-nm and 1064-nm beams; in addition the InSb detectors had a cut off at 5.4 µm, thus effectively behaving as a broad-band filter.

The detectors used (KISDP-1-J1 from Kolmar Technologies, Inc,) were InSb detectors with an active area of 0.01 cm^2. The responsivity of both detectors was matched within 5% of each other; the responsivity at peak wavelength was 3.93 A/W. To avoid electrical noise, this model included an integrated transimpedance amplifier. These detectors were cooled with liquid nitrogen to operate at 77 K. The bandwidth of these detectors was 5 MHz nominal at -3 dB and the detection limit $D^* = 6.2 \times 10^{10}\,\mathrm{cm\,(Hz)^{1/2}/W}$. This corresponds to a noise-equivalent-power (NEP) of 4 nW; this NEP is at least 20 times smaller than the generated mid-IR radiation (see Table 1.) The use of cryogenically cooled detectors is convenient but not a limiting factor in the development of the CO-sensor. Currently, there are commercially available detectors that are thermoelectrically cooled and offer detectivities

Experimental Situation	Test CO Transition Name	Position [cm^{-1}] (μm)	mid-IR generated power [μW]	Diode ID	ECDL Wavelength [nm]	Power [mW]
CO_2 gas cell measurements$^{\#}$	–	2332.990 (4.286)	2.380	JJ82	852.831	80.0
Room-temperature gas cell	$R(23)$	2224.7127 (4.494)	0.897	JJ82	860.782	58.0
Well Stirred Reactor (WSR)	$R(11)$	2186.6390 (4.573)	0.089*	2624	863.612	32.3
Hydrogen/air CO_2-doped flame	$P(19)$	2064.3969 (4.844)♧	0.134	2624	872.826	14.4

\# ECDL settings, as delivered

* Output face of the PPLN crystal was chipped

♧ For this wavelength, the ECDL grating was severely tilted, affecting the cavity performance and beam shape

TABLE 1 Experimental parameters of the CO-sensor for the experiments presented in this study

of $D^* = 1 \times 10^{10}$ cm (Hz)$^{1/2}$/W [27] for which the shot-noise limit is well under the system performance.

An optical chopper, controlled at 500 Hz, was placed in the path of one of the fundamental beams. The signals from the InSb detectors were processed using lock-in amplifiers (Stanford Research Systems SR830) referenced to the synchronization signal from the optical chopper. The use of the lock-in amplifiers improved the signal-to-noise ratio (SNR) by rejecting the noise components with frequencies different than the chopper frequency. For a mid-infrared power of 250 nW incident on the signal detector, the use of phase-sensitive detection reduced the noise by a factor of three as compared to directly reading the detector signal. The output of the lock-in amplifier was recorded using a computer-controlled digital oscilloscope (Tektronix TDS 3014).

The ECDL was delivered with an optimized wavelength of 852.831 nm and a power output of 80 mW. With this configuration the initial system produced 2.3 μW at 4.286 μm. Later, a diode laser with output centered at 862 nm was purchased and installed in the ECDL assembly. With these two diodes, the ECDL wavelength was coarse tuned within the range 852.8–872.8 nm. Table 1 summarizes the sensor configuration and operating characteristics for the measurements discussed in this paper. In this range the DFM output radiation was close to resonance with transition lines in the R- and P-branch of the fundamental CO band. Lines tested in the spectral range 4.49–4.84 μm included the $R(25)$, $R(24)$, $R(23)$, $R(20)$, $R(11)$, $P(18)$, and $P(19)$ transitions, as listed in Table 2.

2.2 *Data processing*

In general, data processing refers to the comparison of the measured absorption spectrum with the theoretical prediction of Beer's law:

$$\frac{I(\omega,0)-I(\omega,l)}{I(\omega,0)} = 1-\exp(-k_\omega l)\,, \tag{1}$$

where l is the path length, $I(\omega,0)$ and $I(\omega,l)$ are the spectral intensities at zero and l, respectively, and k_ω is the spectral absorption coefficient given by the product of the line strength and the line profile which accounts for broadening [28]. A computer code for the analysis of the absorption spectrum was developed. For calculation of the absorption spectrum, the line shape was assumed to be a Voigt profile. The Voigt profile was computed using the routine developed by Humlicek [29]. The absorption code incorporates spectroscopic line parameters from the HITRAN/HITEMP database for CO and CO_2, which is an update to the HITRAN96 database [30]. The HITRAN database was updated in 2001 and 2004. The spectral line parameters for the CO molecule were not changed from the 1996 version in the first update [31]. For CO in the fundamental band, the 2004 HITRAN

	$\omega_{o\tau}$ [cm^{-1}]	[μm]	$S_\tau(296)$ [cm^{-1}/molecule cm^{-2}]	γ^0_{CO-air} [cm^{-1}/atm]	γ^0_{CO-CO} [cm^{-1}/atm]	$E_{\eta''}$ [cm^{-1}]	n
$R(25)$	2230.5258	4.483	5.895×10^{-21}	0.0440	0.0500	1247.0592	0.69
$R(24)$	2227.6386	4.489	9.011×10^{-21}	0.0445	0.0505	1151.3150	0.69
$R(23)$	2224.7127	4.494	1.350×10^{-20}	0.0450	0.0510	1059.3718	0.69
$R(20)$	2215.7044	4.513	4.018×10^{-20}	0.0480	0.0537	806.3828	0.69
$R(11)$	2186.6390	4.573	3.314×10^{-19}	0.0579	0.0634	253.6672	0.69
$P(18)$	2068.8469	4.833	6.601×10^{-20}	0.0522	0.0578	656.7892	0.69
$P(19)$	2064.3969	4.844	4.880×10^{-20}	0.0513	0.0565	729.6774	0.69
$P(13)$*	2064.5839	4.843	1.282×10^{-23}	0.0574	0.0623	2489.7831	0.69

* This is a hot-band transition from $v'' = 1$ to $v' = 2$, and it can only be detected at high temperatures

TABLE 2 Spectroscopic parameters retrieved from HITRAN database [30] for some selected transitions in the fundamental band of $^{12}C^{16}O$. These transitions (τ) correspond to $v'' = 0$ to $v' = 1$ with $\Delta J = \pm1$

update has improved the accuracy of the collisional broadening coefficients from 2–5% in the 1996 version to 1.3–2.5% of experimental values [32].

The code was designed to calculate the absorption spectrum of CO and CO_2 in a given spectral region using temperature, pressure, path length, and gas-mixture composition as input parameters. It is necessary to consider the gas-mixture composition because of the effect of other species on the collisional broadening of CO. HITRAN provides the coefficients for self- (CO−CO; $\gamma^{o}_{\text{CO-CO}}$, in $\text{cm}^{-1}/\text{atm}$) and air- (CO−air; $\gamma^{o}_{\text{CO-air}}$, in $\text{cm}^{-1}/\text{atm}$) collisional broadening at 296 K, as well as the coefficient n of temperature dependence of the air-broadened halfwidth. The collisional broadened half-width at half-maximum (HWHM) [$\gamma(T, P)$] is calculated as suggested by Rothman et al. [30] by

$$\gamma(T, P) = \left(\frac{296}{T}\right)^{n} \left[\gamma^{o}_{\text{CO-air}}(P - P_{\text{CO}}) + \gamma^{o}_{\text{CO-CO}} P_{\text{CO}}\right] , \quad (2)$$

where T [K] is the gas temperature, P [atm] is the total mixture pressure, and P_{CO} [atm] is the partial pressure for CO.

In the combustion of hydrocarbon fuels, it is reasonably assumed that the molecular composition of the products will be dominated by water, carbon dioxide and nitrogen; none of which is properly accounted for by (2). Proper computation of the collisional broadening of CO requires knowledge of the flame composition and for the target CO transition, the collisional broadening coefficient ($\gamma^{o}_{\text{CO-species}}$) of CO by every species present in the mixture. To account for the collisional broadening by other species, the correction factors G_{CO} and G_{CO_2} were introduced to correct the collisional width calculated from the HITRAN parameters. $\gamma(T, P)$ is multiplied by the correction factor G_{CO} and the collisional linewidth $\Delta\nu_c$ [cm^{-1}] full-width at half-maximum (FWHM) is calculated by (a similar equation applies for CO_2 absorption)

$$\Delta\nu_c = 2 \cdot \gamma(T, P) \cdot G_{\text{CO}} \quad (3)$$

$G_{\text{CO}} = 1$ corresponds to a gas mixture composed of CO and synthetic air (79% N_2 and 21% O_2). The G_{CO} factor is used as a fitting parameter in the absorption code and to verify the code performance a series of gas-cell measurements were carried with CO/N_2 mixtures. In these measurements, G_{CO} corrected for CO−N_2 broadening as opposed to CO−air; results are shown in Sect. 3.1. It is important to emphasize that the behavior of G_{CO} is very complex since it is dependent on the mixture composition and the particular CO transition being interrogated.

By varying the input parameters, the theoretical absorption spectrum that is the best-fit to the experimental absorption spectrum is found. Depending on the particular experimental conditions, some parameters were known and fixed. The remaining parameters were adjusted in two steps. An evolutionary algorithm [33, 34] was performed for 50 generations with 100 sets per generation. Subsequently, the Levenberg–Marquardt method [35, 36] was applied, initialized by the best-parameters set found by the evolutionary routine.

To assess the sensor detection limit, the rms value of the best fit was calculated. The root-mean-square (rms) refers to the square root of the mean squared deviation of the measured absorption spectrum from the best fit value. The detection limit was defined for the signal-to-noise (SNR) ratio of one, and the noise quantified by the rms value is an indication of the minimum detectable absorption. To evaluate the detection limit for the sensor, this rms value is considered to be equal to the peak absorption for a given transition under combustion conditions (i.e., CO/air mixture at atmospheric pressure and temperature of 1000 K) for a standard path length of one meter. This standard definition of the detection limit provides a means for comparison of the performance of the sensor under different experimental conditions.

3 Experimental results

The CO-sensor has been tested in a well-controlled room-temperature gas cell and flames in the laboratory. It has also been successfully tested in realistic combustion environments such as the exhaust stream of a well-stirred reactor (WSR).

3.1 *Measurements in the room-temperature gas cell*

The initial set of CO-absorption measurements was performed in a 30-cm-long gas cell at room-temperature. The cell was filled with known concentrations of CO diluted in nitrogen at various pressures. Room-temperature gas-cell measurements were initially performed to demonstrate the sensor operation and to check the performance of the theoretical code. Numerous CO transitions were investigated in order to identify those that avoid interferences from CO_2 and H_2O molecules at high temperature. For each of these transitions, experiments were performed first in the room-temperature gas cell to confirm the wavelength of the ECDL and the HITRAN/HITEMP spectroscopic line parameters.

For the initial gas-cell measurements, the ECDL grating was tuned using a 1.3-Hz sawtooth function. As a result of this scanning of the grating, the generated mid-IR frequency is tuned back and forth across the absorption feature. Two absorption traces shown in the figures as “Absorption 1” and “Absorption 2” are thus obtained. For these direct-absorption experiments, eight scans were acquired in 3.0 s and averaged using the digital oscilloscope. The Tektronix digital oscilloscope has a resolution of 10 000 data points, and binning 10 neighboring data points in software reduced the read noise. It was verified that this binning process did not affect the spectral line shapes.

Hanna et al. [25, 37] describe the basic data-analysis technique used in our CO-absorption work. For gas-cell measurements Hanna et al. acquired the signal and reference traces for absorbing conditions in the gas cell. The cell was then evacuated and filled with clean air, then signal and reference traces were acquired again. The spectral transmission was then obtained by dividing the ratio of the signal to the reference traces under absorbing conditions by the ratio of the signal to the reference traces under non-absorbing conditions (cell filled with air). This technique requires a measurement with non-absorbing gas in the test region. In some experimental situations, such as in the exhaust of a gas turbine engine, it is not possible or feasible to turn the engine on and off. Under these conditions a slightly different scheme was used. The unattenuated portions of the signal scan [$I(\omega, l)$] were fit using a third-degree polynomial [$p(\omega)$]. To compute the

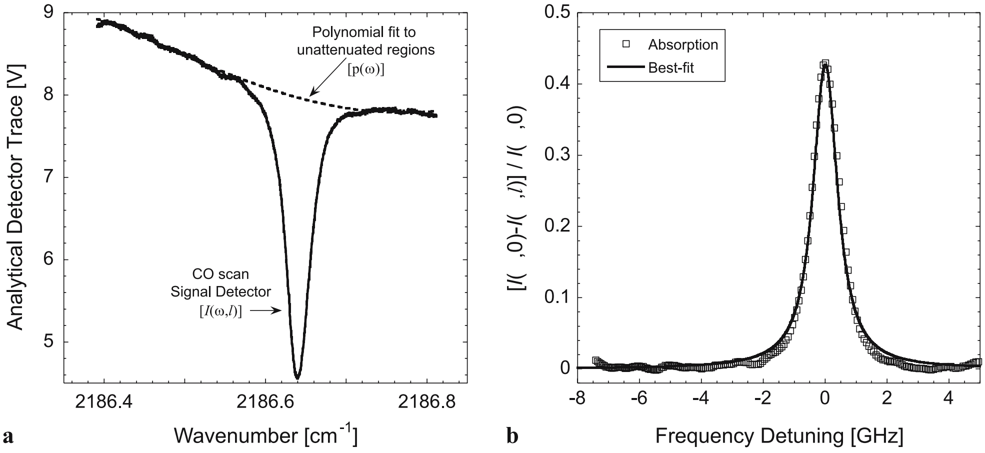

FIGURE 2 Normalization scheme. Panel (**a**) signal detector traces acquired for the absorbing conditions of the test region and the polynomial fit to the unattenuated portions of the signal trace. (**b**) The resulting absorption with its best-fit theoretical shape

third-degree polynomial, the unattenuated regions must be distinguishable from the regions with absorption features and the scanning range of the system must be large enough to resolve the wings of the transition line.

Figure 2a shows the raw CO transmission data recorded from the signal detector. The unattenuated regions for the trace were identified between 2186.4 to 2186.54 cm^{-1} and 2186.74 to 2186.82 cm^{-1}. Figure 2a includes the fitted polynomial to the unattenuated regions. The absorption in Fig. 2b was computed using

$$\frac{I(\omega,0)-I(\omega,l)}{I(\omega,0)} = 1 - \frac{I(\omega,l)|_{\text{CO}_\text{scan}}}{p(\omega)} . \quad (4)$$

The scanning range of the ECDL in the CO-sensor system allowed the determination of unattenuated regions of the absorption scans. The polynomial fit technique was employed for the gas-cell measurements.

Figure 3 shows experimental and theoretical spectra for the $R(23)$ transition of the fundamental band of CO at 2224.7127 cm^{-1} when the gas cell was filled with a mixture of 1010 ppm CO in a buffer gas of N_2 at pressures of 6.66 kPa and 13.33 kPa. The specific operating conditions for the sensor are listed in Table 1. This gas mixture was prepared by Matheson as a “certified standard” with an accuracy of 2%. The gas cell was at room temperature, and the best fit of the data corresponds to an average theoretical CO concentration of 1004 ppm. The estimated uncertainty in the experimental measurements for the CO concentration is less than 20 ppm or 2% of the CO mole fraction of 1010 ppm. This estimate is indicative of the best-fit concentration values obtained from a series of experiments performed on different days and for different transitions. The experimental uncertainty is in part due to the uncertainties of the pressure gage, uncertainties in the theoretical model, and baseline level fluctuations due to long-term drifts in laser power or optical alignment. This experimental value is still in good agreement with the certified gas-mixture concentration, and, as can be seen on Fig. 3, the theoretical spectral line shape, intensity, and line width are in excellent agreement with the experimental line shape.

For the gas-cell measurements, the rms noise in the baseline was measured to be 0.0017, which corresponds to a noise detection limit of 1.1 ppm per meter path length in gas at combustion conditions i.e., 1000 K and 1 atm. This assumes a signal-to-noise (SNR) ratio of 1 at the detection limit.

The HITRAN [30] database shows that the CO-absorption lines in the R branch of the fundamental band are separated by approximately 3 cm^{-1}, which is larger than the mode-hop-free tuning range of the ECDL. It was not possible to scan over two neighboring CO transitions, and it was, therefore, difficult to verify the wavelength of the generated mid-IR beam. By adding CO_2 to the CO/N_2 mixture in the gas cell, some weak

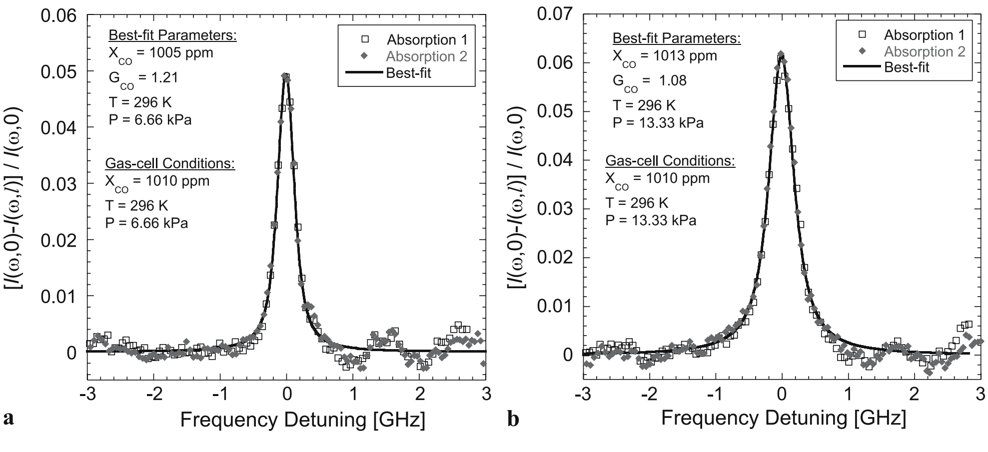

FIGURE 3 Comparison of the measured and calculated $R(23)$ transition in the fundamental band of CO at 2224.7127 cm^{-1}. The 0.32-m-long, room-temperature gas cell was filled with a mixture of 1010 ppm CO and N_2 at pressures of (**a**) 6.66 kPa and (**b**) 13.33 kPa

CO_2 transitions appeared within the mid-IR scanning range. The resulting spectrum included both CO and CO_2 transitions, and the wavelength of the DFM-generated mid-infrared radiation was thus verified.

Several $CO/N_2/CO_2$ mixtures were probed in a series of room-temperature experiments in the gas cell. Two of the resulting spectra are shown in Fig. 4. The $R(23)$ transition of CO is shown at 0 GHz frequency detuning, while the absorption line observed at approximately −6 GHz corresponds to the CO_2 transition $P(51)$ at $2224.519\,\mathrm{cm}^{-1}$. In this experiment the gas cell was filled with a mixture of CO/N_2 until the gas-cell pressure reached 13.33 kPa. CO_2 was then added until the gas-cell pressure reached 14.66 or 22.66 kPa. For a final pressure of 14.66 kPa, the mixture composition was 918 ± 30 ppm, 90.8 ± 2.3%, and 9.09 ± 2.3% for CO, N_2, and CO_2, respectively. For the final pressure of 22.66 kPa, the concentrations of CO, N_2 and CO_2 were calculated to be 594 ± 18 ppm, 58.7 ± 1.3%, and 41.17 ± 1.3% respectively. The uncertainties in these calculations were based on the estimated accuracy of the pressure transducer and the published uncertainty in the composition of the certified mixture. From the spectra shown in Fig. 4, it is evident that the agreement between measured and theoretical line positions, intensities, and concentrations falls within the estimated experimental uncertainties.

For the gas-cell measurements, the correction factor G_{CO} accounts for the fact that nitrogen (N_2) is the buffer gas and not air as assumed in the HITRAN-based absorption code. From a series of measurements on transition $R(23)$ in the gas cell, the average of the best-fit G_{CO} value was 1.11. With this G_{CO}, the N_2-broadened halfwidth coefficient ($\gamma^{o}_{CO-N_2}$) was calculated to be $0.0502\,\mathrm{cm}^{-1}/\mathrm{atm}$. This value is 2.41% lower than the value reported by Varghese and Hanson [11], but 3.43%, 7.18%, and 6.25% higher than the values from Hartmann et al. [38], Predoi-Cross et al. [39], and Sinclair et al. [40] respectively.

For the $CO/N_2/CO_2$ mixture experiments the average best-fit value of G_{CO} was 1.093, thus accounting for the inclusion of CO_2 in the mixture. By using the measured $\gamma^{o}_{CO-N_2}$ for $R(23)$ the CO_2-broadened halfwidth coefficient ($\gamma^{o}_{CO-CO_2}$) was calculated to be $0.0461\,\mathrm{cm}^{-1}/\mathrm{atm}$. This number agrees within 4.3% of the value computed by Hartmann et al. [38] of $0.0465\,\mathrm{cm}^{-1}/\mathrm{atm}$, obtained by interpolation for $J = 23$. Experimental data for the $\gamma^{o}_{CO-CO_2}$ value have been published [41–43] for CO lines in the fundamental band for $J \leq 19$. Our measurements for $\gamma^{o}_{CO-CO_2}$ cannot be directly compared.

3.2 *Measurements in the exhaust of a well-stirred reactor (WSR)*

In order to demonstrate the sensor in a more realistic combustion environment, CO-measurements were performed in the exhaust stream of a well-stirred reactor (WSR) at Wright-Patterson Air Force Base (WPAFB). The CO-sensor was mounted on a 0.6-m by 1.2-m optical breadboard, and an aluminum enclosure was built to shield the optics from the environment (i.e., particles, heating, radiation). During testing, a flow of dry air was directed into the enclosure to maintain a stable operating temperature. Vibrations were reduced by mounting the sensor on an optical bench and vibration isolation pads.

The exhaust gases from the WSR exited through a 5-cm-diameter, 30-cm-long ceramic tube. The mid-infrared beam was directed along the diameter of the tube approximately 3 mm above the tube exit. A B-type thermocouple with 0.02-mm-diameter wires was placed in the exhaust at the same height as the beam but about 4 mm to the side. An extractive probe was located in the center of the exhaust stream approximately 2 cm above the beam height. The probe was operated in conjunction with non-dispersive IR (NDIR) analyzer (VIA 510 from Horiba Instruments). The uncertainty of this probe-analyzer system was estimated to be 3%. With this instrumentation, the diode-laser-based measurements were compared with the data from extractive sampling.

High-temperature spectral calculations were performed using the HITRAN database, and it was observed that the presence of CO_2 introduces significant spectral interference for the CO fundamental band R-branch transitions for J values higher than 14. To avoid CO_2 interferences, the $R(11)$ CO transition at $2186.6390\,\mathrm{cm}^{-1}$ was selected for the absorption measurements. The 852-nm ECDL was coarse-tuned to 863.612 nm to achieve mid-IR generation at $2186.6390\,\mathrm{cm}^{-1}$ (see Table 1). The 852-nm diode laser in the ECDL was replaced with an 862-nm diode. The new diode was operated at 863.612 nm with 32.3 mW and exhibited

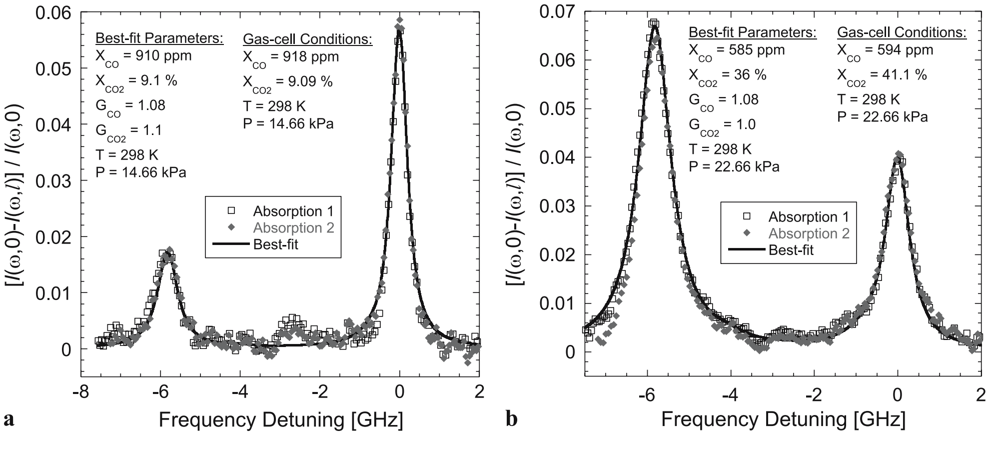

FIGURE 4 Comparison of the measured and calculated absorption for the CO transition $R(23)$ can be observed at 0 GHz frequency detuning. The absorption line observed at approximately −6 GHz corresponds to the $P(51)$ transition from the CO_2 molecule at $2224.519\,\mathrm{cm}^{-1}$. For these experiments the 0.32-m-long gas cell was filled with a mixture of $CO/N_2/CO_2$ at labeled concentrations for pressures (**a**) 14.66 kPa and (**b**) 22.66 kPa

a mode-hop-free tuning range of 14 GHz. With this power, the expected mid-IR power was calculated to be 410 nW, a power drop of 46% based on the mid-infrared power of 900 nW obtained using 58 mW from the ECDL at 860.782 nm. The mid-infrared power obtained using the 863.612 nm ECDL was 89 nW, almost a factor of five lower than expected. A small chip in the PPLN crystal face was discovered at the WSR facility during alignment of the CO-sensor, and this was later determined to be the primary cause of the low mid-infrared power.

Given the operational conditions of the reactor, the CO-absorption transitions were broadened to the extent that the spectra did not exhibit any regions where attenuation was negligible, and it was not possible to perform a good polynomial fit for $I(\omega,0)$. The oscilloscope trace of the reference detector was used in the data-reduction process to determine $I(\omega,0)$. To account for the background flame emission, the half-wave plate in the 1064-nm beam path was detuned ($\Delta\varphi$) 45° so that the mid-IR generated in the PPLN was completely cancelled. The oscilloscope trace recorded for this condition served as the baseline for the signal and reference detectors. The difference between signal-detector $[I(\omega,l)]$ trace and its baseline $[I(\omega,l)|_{\Delta\varphi=45^\circ}]$ was normalized by the difference between the reference-detector $[I'(\omega,0)]$ trace and its baseline $[I'(\omega,0)|_{\Delta\varphi=45^\circ}]$. In general, the output of the lock-in amplifier was different for the signal and reference traces, and it was necessary to include a scaling factor in the expression for the absorption. This factor is the ratio in the denominator of the right-hand side of

$$\frac{I(\omega,0)-I(\omega,l)}{I(\omega,0)} = 1-\frac{I(\omega,l)-I(\omega,l)|_{\Delta\varphi=45^\circ}}{\left\|\begin{array}{c}\left[I'(\omega,0)-I'(\omega,0)\big|_{\Delta\varphi=45^\circ}\right]\\ \times\frac{I(\omega_1,l)-I(\omega_1,l)|_{\Delta\varphi=45^\circ}}{I'(\omega_1,0)-I'(\omega_1,0)|_{\Delta\varphi=45^\circ}}\end{array}\right\|} \tag{5}$$

where ω_1 is the frequency at which $I'(\omega,0)$ is maximum. By using this scaling factor, the reference detector trace was projected as the trace of the signal detector when no absorption occurs. This technique assumes that the shapes of the signal and reference traces were the same if no absorption occurred. It was found that the unattenuated signal trace and the reference trace were equal to better than 1% over the entire spectral scan. Therefore the error induced by this data-processing scheme was minimal.

Figure 5 shows the comparison of the measured and calculated CO-absorption line shape for the $R(11)$ transition in the fundamental band at 2186.6390 cm^{-1}. The reactor was operated using ethylene at equivalence ratios of $\Phi = 1.40$ and $\Phi = 1.75$. Due to high CO concentration, almost 100% of the signal beam was absorbed at the line center. Measurements could not be made at lower levels of CO because of operational limitations of the WSR. Due to thermal considerations, the WSR can only be operated at very fuel-lean ($\Phi = 0.4$ to 0.75) or very fuel-rich ($\Phi = 1.4$ to 1.75) conditions. At lean operating conditions, the CO concentration was expected to fall in the range 30 to 60 ppm, with CO_2 levels within 6 to 7%. Under these conditions, spectral interference from CO_2 was strong enough to obscure the CO transitions. The low signal-to-noise ratio of the measurements due to the low mid-infrared power and the short path length through the flame were also factors in our inability to observe the CO transition under fuel-lean conditions.

For the fuel-rich conditions, the only visible species in the recorded spectra was CO. While CO_2 is present in the exhaust stream, its concentration was comparable to the CO concentration, and the intensity of the CO_2 transitions in this spectral region are two orders of magnitude smaller than those for CO. The CO_2 concentration, thus, has no effect on the fitting procedure. The CO concentrations determined from the best-fit theoretical parameters for experimental curves obtained from several absorption scans under different fuel-rich conditions agreed to within 15% with the results obtained from the extractive probe in conjunction with a NDIR analyzer. Similar discrepancies between probe and diode-laser measurements have been reported previously by Schoenung and Hanson [44], although Nguyen et al. [45] have reported that extractive sampling probes underestimate CO concentration by a factor of 10.

The temperatures reported in Fig. 5 are the readings from the thermocouple and were not corrected for radiation because the thermocouple was located at a different position than the beam path. They were only used as an initial guess for the best-fit procedure. The resulting best-fit temperatures were consistent to within 100 K for the WSR experiments. Notice that for the best fit on Fig. 5, the G_{CO} factor is larger

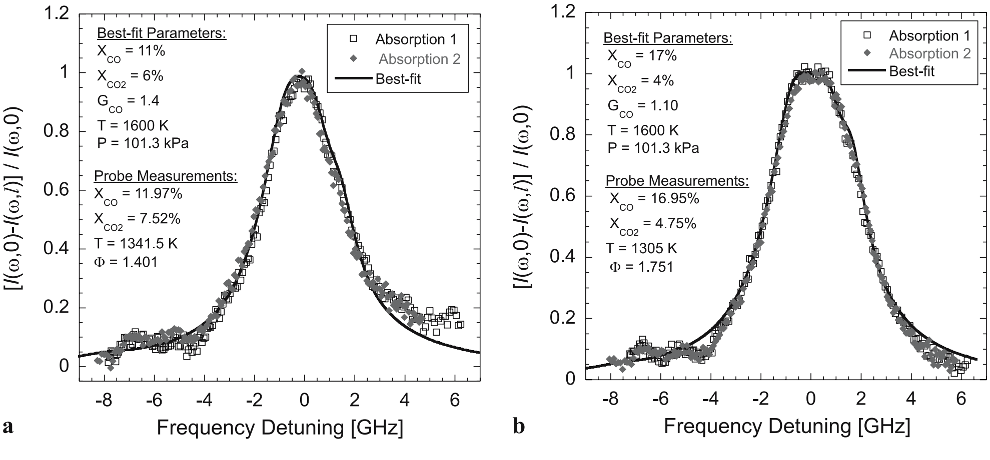

FIGURE 5 Comparison of the measured and calculated CO-absorption line shape for the $R(11)$ transition in the fundamental band at 2186.6390 cm^{-1}. Measurements were performed 3 mm over the exhaust of the WSR at WPAFB over an absorption path length of 5 cm. Reactor was run fuel-rich (**a**) $\Phi = 1.401$ and (**b**) $\Phi = 1.751$

than 1 and accounts for line broadening by species other than CO and air. Notice also that the G_{CO} is reduced as expected when the CO_2-to-CO concentration ratio decreases towards higher equivalence ratios.

For the WSR measurements, the intrinsic noise to the best fit (rms) was calculated to be 0.039. This corresponds to a detection limit of 21 ppm-m for gas at 1000 K, assuming a SNR of 1. The decrease in sensitivity during the field measurements is due in part to noise and vibrations from the combustion equipment. However, the low value of the generated mid-IR power due to the chipped PPLN crystal was the most significant factor in the increase of the detection limit.

3.3 *Measurements in* $H_2/air/CO_2$ *flames*

CO measurements were also performed in near adiabatic $H_2/air/CO_2$ flames to investigate high-temperature CO_2 interferences in detail and identify CO lines with minimal interferences. The detection of CO in high-temperature hydrocarbon/air flames using diode-laser probes has been reported by many groups [10, 12, 44, 46, 47]. CO concentrations in these flames are adjusted by controlling the equivalence ratio. CO concentrations in the range of 1% to 15% are measured, and at the edge of the flames the CO concentrations are the lowest. Recently, Wehe et al. [16] used a rich hydrogen/air diffusion flame to simulate the exhaust of a gas turbine. Their flame was cooled with added nitrogen to achieve a temperature of approximately 1150 K, measured with a thermocouple. CO_2 was seeded into the burner and CO was formed by dissociation. In this flame Wehe et al. reported a measurement of 27 ppm of CO in a 1.2-m folded path length using a quasi-cw quantum-cascade laser at 4.62 μm.

In the current study, a $H_2/air/CO_2/N_2$ flame was stabilized on a Hencken burner. The flame produced by the Hencken burner is flat, uniform, steady, and nearly adiabatic [48]. A hydrogen/air flame with added CO_2 and N_2 allows for adjustment of the CO concentrations by varying the CO_2 flow and adjustment of the flame temperature by varying the N_2 flow. This flame was ideal for testing of the CO-sensor since in addition to controlling the CO concentration it also offered a high temperature environment with a high concentration of CO_2.

To perform CO-concentration measurements in the flames, the ECDL was coarse tuned to 872.826 nm so that the generated mid-IR radiation was in resonance with the $P(19)$ transition in the fundamental vibrational band of CO at $2064.3969\,cm^{-1}$ [30]. Tuning the mid-IR radiation to the wavelength of this particular transition was advantageous because of the absence of CO_2 absorption lines in this region. Furthermore, within the scanning range of the sensor the $P(13)$ transition of the v:2 $\leftarrow$ 1 band at $2064.583\,cm^{-1}$ emerges at high temperatures, offering independent verification of the mid-IR wavelength and the opportunity for performing two-line thermometry.

To address the P branch, some modifications to the sensor layout were performed. A different PPLN crystal with

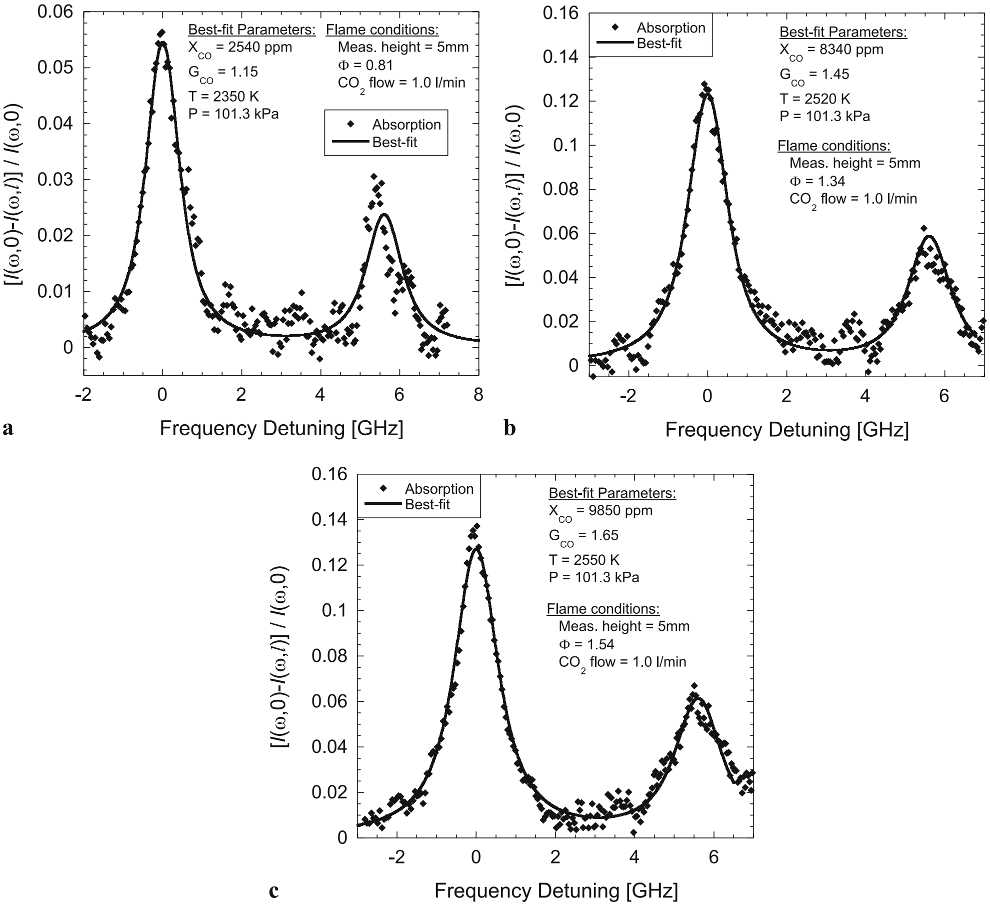

FIGURE 6 Comparison of measured and calculated CO-absorption line shapes for the $P(19)$ (at 0 GHz) transition in the fundamental band at $2064.3969\,cm^{-1}$ and the $P(13)$ (at 5.5 GHz) transition of the v:2 $\leftarrow$ 1 band at $2064.583\,cm^{-1}$ [30]. CO-absorption measurements were performed at 5 mm from the surface of the Hencken burner through a path length of 5 cm. The equivalence ratio of these flames is (**a**) $\Phi = 0.81$, (**b**) $\Phi = 1.34$, and (**c**) $\Phi = 1.54$. The composition of the hydrogen/air flames is given in Table 3. For these flames the inlet CO_2 flow is 1.0 l/min

Φ	Burner inlet flows [l/min]				X_{CO_2}	X_{CO} [ppm]	Fig.
	H_2	Air	N_2	CO_2	[%]*	(meas. at 5 mm)	
0.81	25	72	0	1	1.02	2540	6a
1.15	23	65	28	2	1.69	4500	7a
	23	65	28	3.5	2.93	5820	7b
	23	65	28	4.9	4.06	9400	7c
1.34	40	85	20	1	0.68	8340	6b
	40	85	20	2	1.36	7040	–
	40	85	20	3	2.03	11 900	–
1.54	32.3	67.9	28.8	1	0.77	9850	6c
	32.3	67.9	28.8	1.9	1.45	7220	–
	32.3	67.9	28.8	2.5	1.90	9990	–
	32.3	67.9	28.8	3.4	2.57	15 790	–

* Calculated mole fraction of carbon dioxide in the reactants

TABLE 3 Composition of the flames stabilized in the Hencken burner

a quasi-phase-match period of 22.1 μm was used to achieve DFM generation in the 4.8-μm region. The ECDL grating was severely tilted in order to obtain laser radiation at 872.862 nm from the diode laser with a nominal wavelength of 862 nm. The severe tilting of the grating caused the power of the ECDL to decrease to 14.4 mW while the shape of the beam was distorted. The ECDL tuning capabilities were degraded so that the scanning frequency was reduced to 260 mHz to obtain about 9 GHz of single-mode hop-free tuning range in only the region of the scan where the laser frequency was decreasing. Under these conditions the generated beam at 4.8 μm had a power of 134 nW as compared to 2.38 μW at 4.2 μm (see Table 1). For the flame measurements, data were acquired for a time period of 13.4 s. Typically, seven traces were consecutively acquired and averaged by the software. Binning of ten neighboring data points was performed to reduce oscilloscope read noise.

Due to the limited scanning range and the presence of two CO transitions, the recorded spectra acquired using the signal detector did not exhibit any regions with negligible attenuation needed to perform a polynomial fit for $I(\omega, 0)$. Instead of a polynomial fit, the signal detector was used to record $I(\omega, 0)$ since the burner can be easily extinguished and then reignited. The flame was ignited and data were recorded with the signal detector $[I(\omega, l)]$. To account for flame emissions, the mid-IR generation was cancelled (see Sect. 3.2) and the baseline spectrum was acquired $[I(\omega, l)|_{\Delta\varphi=45^\circ}]$. The baseline was subtracted from the signal trace. Then the flame was extinguished and an oscilloscope trace of the signal detector was acquired with no flame and no CO in the test region (similar concept as in Hanna et al. [25]). Absorption was then calculated using

$$\frac{I(\omega,0)-I(\omega,l)}{I(\omega,0)} = 1 - \frac{\left[I(\omega,l)-I(\omega,l)|_{\Delta\varphi=45^\circ}\right]_{\text{flame}}}{\left[I(\omega,l)-I(\omega,l)|_{\Delta\varphi=45^\circ}\right]_{\text{no-flame}}} . \tag{6}$$

A series of CO-concentration measurements were performed in different flames as described in Table 3. The flames were stabilized at equivalence ratios of $\Phi = 0.81$, 1.15, 1.34, 1.54

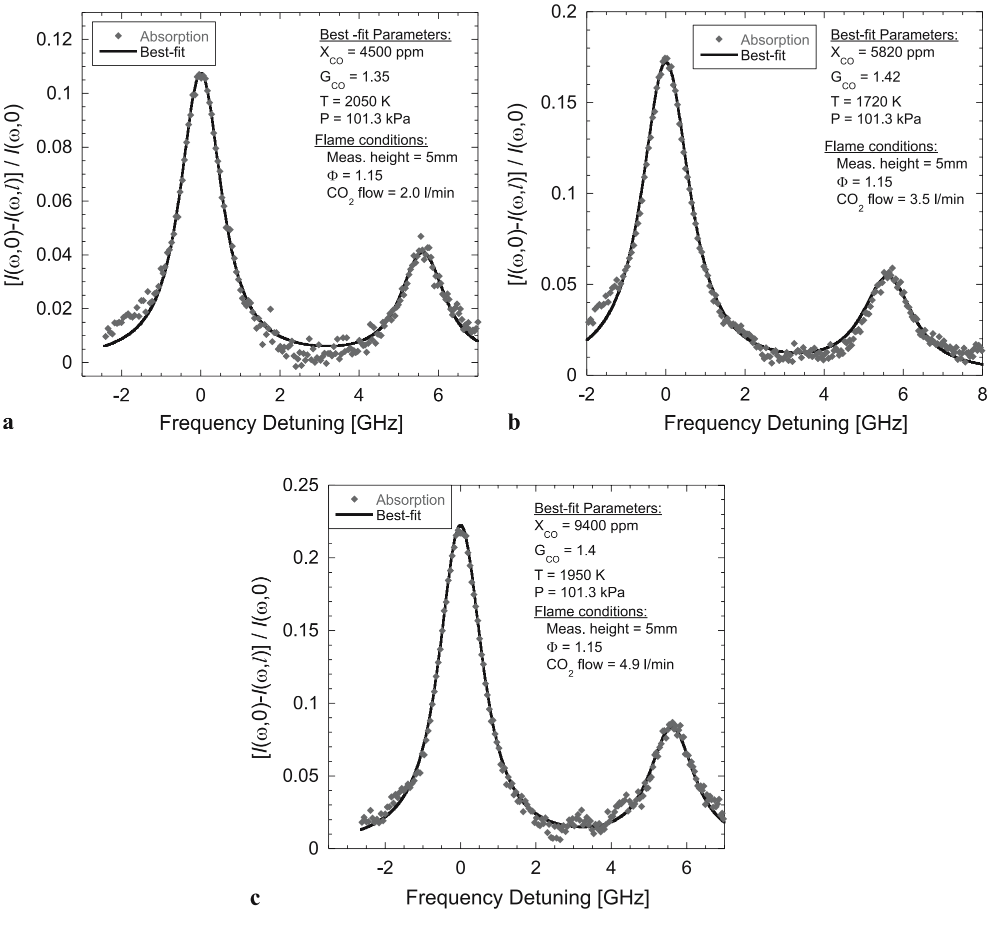

FIGURE 7 Comparison of the measured and calculated CO-absorption line shapes for the $P(19)$ (at 0 GHz) transition in the fundamental band at 2064.3969 cm^{-1} and the $P(13)$ (at 5.5 GHz) transition of the v:2 ← 1 band at 2064.583 cm^{-1} [30]. Measurements were performed 5 mm above the surface of the Hencken burner in a fuel-rich ($\Phi = 1.15$) hydrogen/air CO_2-doped flame. The path length through the flame was estimated to be 5 cm. Flames composition is given in Table 3. The flow of dopant CO_2 was adjusted to (**a**) 2.0 l/min, (**b**) 3.5 l/min, and (**c**) 4.9 l/min to change the CO content of the flame

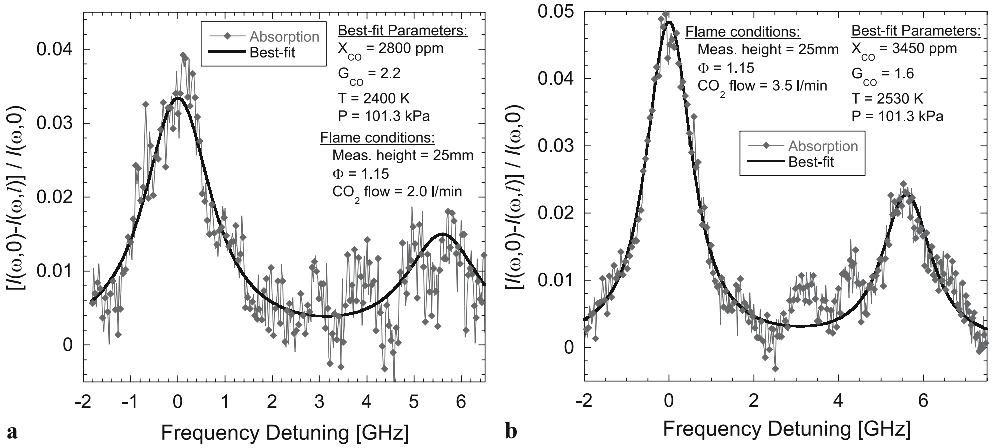

FIGURE 8 Comparison of the measured and calculated CO-absorption line shapes for the $P(19)$ (at 0 GHz) fundamental band transition at 2064.3969 cm^{-1} and the $P(13)$ (at 5.5 GHz) transition of the v:2 ← 1 band at 2064.583 cm^{-1} [30]. Measurements were performed 25 mm above the surface of the Hencken burner. The path length through the flame was estimated to be 5 cm. Panels (**a**), (**b**) compare directly to the corresponding panels of Fig. 7

for CO_2 flow rates of 1.0 to 4.9 standard liters per minute (SLM). For these flames, the diode-laser sensor was used to measure flame CO concentrations in the range of 2540 ppm to 16% at 5 mm from the burner surface.

Figures 6, 7, and 8 show the measured and calculated absorption spectra for the $P(19)$ fundamental band and $P(13)$ v:2 ← 1 band CO transitions at 0 and 5.5 GHz frequency detuning, respectively. Measurements were performed at 5 mm from the burner surface. The absorption path length through the flame was 5 cm, corresponding to a single pass. Figure 6 shows three different flames with equivalence ratios of a) 0.81, b) 1.34, and c) 1.54. For these flames the flow rate of carbon dioxide was 1.0 SLM. The lower measured CO concentration and flame temperature were observed for the flame with $\Phi = 0.81$. The flow rates used to produce the $\Phi = 0.81$ flame were at the limit of the burner stability, and the flame was close to the blow-off limit. Under these conditions the flame was difficult to operate. To achieve stable flames with lower CO concentrations, several fuel–oxidizer ratios were tried. Figure 7 present fuel-rich flames with an equivalence ratio of 1.15. The fuel stream was prepared by mixing 23.0 SLM of hydrogen (H_2) and 28.0 SLM of nitrogen (N_2). The air flow and the CO_2 flow were mixed to form the oxidizer stream. In this series of experiments, the air flow was 65.0 SLM and the CO_2 flow rate was varied from 2.0 to 4.9 SLM.

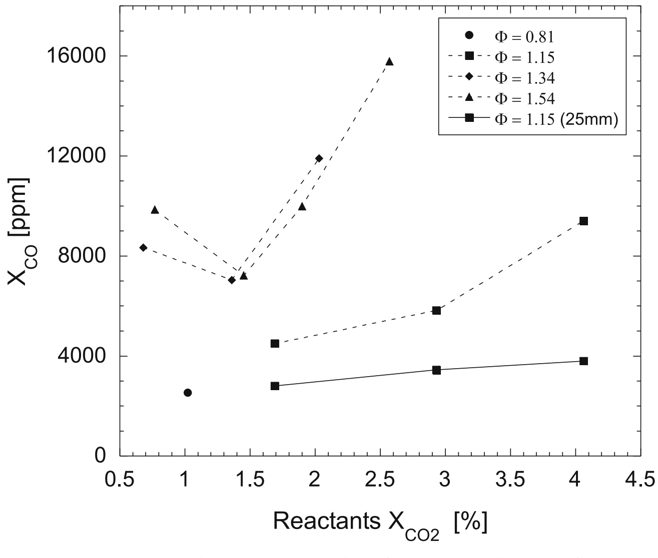

FIGURE 9 Measured CO concentration for the H_2/air/CO_2 flames as a function of the CO_2 mole fraction in the inlet flow. Measurements were performed with the mid-infrared sensor at 5 mm from the top of the burner

Figures 6 and 7 show the comparison of the experimental CO spectrum with the best-fit theoretical spectrum for measurements at 5 mm from the burner surface. As shown in Figs. 6 and 7, the theoretical spectral line shape, intensity, and line width of both absorption features are in excellent agreement with the experimental data. The rms noise standard deviation of the experimental spectrum from the best-fit theoretical spectrum shown in Figs. 6 and 7 was measured to be 0.004. Assuming SNR = 1 the detection limit was computed to be 2.5 ppm-m for gas at 1000 K. Based on the repeatability of the data from several tests under identical flow conditions, the uncertainty of the peak absorption was estimated to be on the order of 10%. For the $\Phi = 1.15$ flame measurements at an axial distance of 5 mm, the G_{CO} parameter had an average value of 1.42. As discussed, the G_{CO} parameter depends on the flame products which in turn are a function of the reactants composition and flame temperature. In Fig. 6, the line-broadening factor varies between 1.15 and 1.65 for different flame compositions.

Measurements were also performed at 25 mm from the surface of the burner. Figure 8 a and b show the recorded spectra at 25 mm for comparison with panels a and b of Fig. 7, respectively. It can be seen that the CO concentration at the 25-mm location dropped approximately 40% from the 5-mm location while the rms noise maintained the same 0.004 value.

Figure 9 summarizes the measured CO concentration in the series of the tested flames. It shows the measured CO concentration at 5 mm as a function of the reactant CO_2 mole fraction. It is observed that for each flame ($\Phi = 1.15, 1.34, 1.54$) the measured CO concentration reaches a minimum and then increases as the inlet CO_2 flow to the burner is increased. Recall that the CO concentration in the combustion products depends on the flame temperature and the availability of carbon dioxide. As the input amount of CO_2 to the flame increases, the flame temperature is reduced and less CO is produced. As more CO_2 is added to the burner, more CO is produced and, as indicated by the sharp gradient in CO concentration for $X_{CO_2} > 1.4\%$, the production of CO is dominated by the availability of CO_2. Numerical simulations of the Hencken burner flames are required to corroborate the measured values of CO concentration and flame temperature.

4 Summary and future work

A diode-laser-based sensor system for mid-infrared single-pass direct-absorption measurements of CO has been demonstrated. The system produces mid-IR radiation in the 4.4–4.8 μm spectral region by difference-frequency mixing of radiation from a near-infrared ECDL and a compact Nd:YAG laser in a PPLN crystal. The system was tested in different experiments that demonstrate its operation and ability to detect CO in $CO/N_2/CO_2$ mixtures, under combustor exhaust conditions, and in high-temperature post-flame regions with high CO_2 concentrations. This paper presents direct absorption measurements of the fundamental band CO transitions $R(23)$, $R(11)$, and $P(19)$ at 2224.7127, 2186.6390, and 2064.3969 cm^{-1} respectively.

For the CO-absorption measurements in the room-temperature gas cell, the uncertainty of the sensor was estimated to be on the order of 2%. The current detection limit of the system in a laboratory environment was computed to be 1.1 ppm for a 1-m path length through 1000 K combustion gas in a laboratory controlled environment. In similar conditions (i.e. 1 m, 1000 K, 101.3 kPa,) the minimum detectable absorbance for the system described by Mihalcea et al. [2] would correspond to a detection limit of 8470 ppm. This is due to the fact that the interrogated transition $R(13)$ in the second overtone is 1000 times weaker that transitions in the fundamental band. By addressing the $R(15)$ CO transition of the first overtone band, the DFB based system described by Wang et al. [6] yielded a minimum detectable absorbance that corresponds to a detection limit of 1.75 ppm at similar conditions. Line $R(15)$ in the first overtone is 10 times weaker than line $R(23)$ in the fundamental band. Wang et al. [6] system used a DFB laser that allows faster scanning and more power (i.e. 20 mW), thus compensating for the weakness of the addressed transition. These comparisons are only for direct absorption measurements whereas, more sophisticated detection schemes improve the detection limit of the instruments.

The CO-sensor system was also successfully tested in a real combustion environment in the exhaust of the well-stirred reactor (WSR) at Wright-Patterson Air Force Base (WPAFB). CO-concentration measurements in the WSR exhaust agreed to within 15% with extractive probe and NDIR measurements. The estimated CO detection limit was 21 ppm-m for gas at 1000 K. The observed drastic increase in the detection limit was directly related to the reduction of generated mid-infrared power. The reduced power was caused primarily by a chip on the PPLN crystal face. The WSR absorption measurements are an excellent demonstration of the operation of the sensor for measurements with short path length through a very high temperature combustion exhaust.

Finally, CO-absorption measurements were performed on near-adiabatic $H_2/\mathrm{air}/CO_2/N_2$ flames. In the 4.8-μm spectral region, spectral interferences of CO_2 and H_2O were investigated in detail and CO transitions with minimal CO_2 spectral interference were identified. The transition $P(19)$ in the fundamental band at 2064.3969 cm^{-1} and the transition $P(13)$ of the v:2 ← 1 band at 2064.5839 cm^{-1} were probed offering the possibility of two-line thermometry, which also reduces the uncertainty in the spectral-fitting process. The experimental and theoretical line shapes and intensities are in excellent agreement. The line broadening parameter was about 40% greater than the value for air at the same temperature. The noise equivalent detection limit for the sensor for the hydrogen/air CO_2-doped flame experiments was determined to be 2.5 ppm-m at 1000 K gas. Numerical simulations of the Hencken-burner flames will be performed for comparison with the absorption measurements.

To enhance the sensitivity of the CO-sensor, an increase in the generated mid-IR power and better noise discrimination are required. Future plans include substitution of the diode laser to improve the mid-IR generation, as well as implementation of wavelength-modulation spectroscopy (WMS) or frequency-modulation spectroscopy (FMS) [49]. To increase the scanning rate and the mode-hop-free tuning range, the use of a DFB laser is required. To access the P-branch of the CO fundamental band by DFM, an 860-nm DFB diode-laser has to be mixed with a 1047-nm Nd:YLF laser source. These two laser sources had been recently substituted into the CO-sensor system described, and CO-concentration measurements have been performed on the exhaust stream of liquid-fueled CFM-56 gas-turbine model combustor at WPAFB. These experiments will be discussed in a forthcoming publication. The simplicity, generality, and relative low cost of the DFM-based CO-absorption sensor strategy described and tested in this study is potentially applicable to numerous other interesting species in the mid-IR spectral region.

ACKNOWLEDGEMENTS The authors would like to thank Scott Stouffer and Mike Arstingstall at Wright-Patterson AFB for their help in performing the WSR exhaust experiments. This research was supported by the Air Force Research Laboratory, Propulsion Directorate, Wright-Patterson AFB through Innovative Scientific Solutions, Inc. under Contract No, F33615-00-C-2020, F33615-03-D-M2329, by the Air Force Office of Scientific Research (Dr. Julian Tishkoff, Program Monitor), and by the U.S. EPA STAR Program under Project No. R-82818001.

REFERENCES

1 R.M. Mihalcea, D.S. Baer, R.K. Hanson, Meas. Sci. Technol. **9**, 327 (1998)
2 R.M. Mihalcea, D.S. Baer, R.K. Hanson, Appl. Opt. **36**, 8745 (1997)
3 D.M. Sonnenfroh, M.G. Allen, Appl. Opt. **36**, 3298 (1997)
4 J.J. Nikkari, J.M. DiIorio, M.J. Thomson, Appl. Opt. **41**, 446 (2002)
5 J. Wang, M. Maiorov, J.B. Jeffries, D.Z. Garbuzov, J.C. Connolly, R.K. Hanson, Meas. Sci. Technol. **11**, 1576 (2000)
6 J. Wang, M. Maiorov, D.S. Baer, D.Z. Garbuzov, J.C. Connolly, R.K. Hanson, Appl. Opt. **39**, 5579 (2000)
7 Sacher Lasertechnik, LLC (Buena Park CA, 2005) [http://www.sacher.de/index.php]
8 Frankfurt Laser Co. (Friedrichsdorf Germany, 2005) [http://www.frlaserco/index.htm]
9 V. Ebert, H. Teichert, P. Strauch, T. Kolb, H. Seifert, J. Wolfrum, Proc. Combust. Inst. **30**, 1611 (2005)
10 P.L. Varghese, R.K. Hanson, J. Quantum Spectrosc. Radiat. Transf. **26**, 339 (1981)
11 P.L. Varghese, R.K. Hanson, J. Quantum Spectrosc. Radiat. Transf. **24**, 479 (1980)
12 J.H. Miller, S. Elreedy, B. Ahvazi, F. Woldu, P. Hassanzadeh, Appl. Opt. **32**, 6082 (1993)
13 H.S. Lowry, C.J. Fisher, J. Quantum Spectrosc. Radiat. Transf. **31**, 575 (1984)
14 R.G. Daniel, K.L. McNesby, A.W. Miziolek, Appl. Opt. **35**, 4018 (1996)

15 A.A. Kosterev, F.K. Tittel, R. Köhler, C. Gmachl, F. Capasso, D.L. Sivco, A.Y. Cho, S. Wehe, M.G. Allen, Appl. Opt. **41**, 1169 (2002)
16 S. Wehe, M.G. Allen, X. Liu, J.B. Jeffries, R.K. Hanson, AIAA Paper No. 2003-0588 (2003)
17 T.J. Kulp, S.E. Bisson, R.P. Bambha, T.A. Reichardt, U.-B. Goers, K.W. Aniolek, D.A.V. Kliner, B.A. Richman, K.M. Armstrong, R. Sommers, R. Schmitt, P.E. Powers, O. Levi, T. Pinguet, M. Fejer, J.P. Koplow, L. Goldberg, T.G. Mcrae, Appl. Phys. B. **75**, 317 (2002)
18 W. Chen, D. Boucher, F.K. Tittel, Recent Res. Dev. Appl. Phys. **5**, 27 (2002)
19 W. Schade, T. Blanke, U. Willer, C. Rempel, Appl. Phys. B. **63**, 99 (1996)
20 T. Kelz, A. Schumacher, M. Nägele, B. Sumpf, H.-D. Kronfeldt, J. Quantum Spectrosc. Radiat. Transf. **61**, 591 (1999)
21 D. Richter, D.G. Lancaster, R.F. Curl, W. Neu, F.K. Tittel, Appl. Phys. B. **67**, 347 (1998)
22 M. Seiter, M.W. Sigrist, Infrared Phys. Technol. **41**, 259 (2000)
23 K.P. Petrov, R.F. Curl, F.K. Tittel, Appl. Phys. B. **66**, 531 (1998)
24 K.P. Petrov, L. Goldberg, W.K. Burns, R.F. Curl, F.K. Tittel, Opt. Lett. **21**, 86 (1996)
25 S.F. Hanna, R. Barron-Jimenez, T.N. Anderson, R.P. Lucht, J.A. Caton, T. Walther, Appl. Phys. B **75**, 113 (2002)
26 T.N. Anderson, R. Barron-Jimenez, J.A. Caton, R.P. Lucht, S. Roy, M.S. Brown, J.R. Gord, T. Walther, I. Critchley, L. Flamand, In Proc. ASME Summer Heat Transfer Conference HT2003-47532 (2003)
27 VIGO System S.A. (Warsaw Poland, 2005) [http://www.vigo.com.pl]
28 R.P. Lucht, R.C. Peterson, N.M. Laurendeau, *Fundamentals of Absorption Spectroscopy for Selected Diatomic Flame Radicals* (School of Mechanical Engineering, Purdue University, West Lafayette, Indiana, 1978)
29 J. Humlicek, J. Quantum Spectrosc. Radiat. Transf. **21**, 309 (1979)
30 L.S. Rothman, C.P. Rinsland, A. Goldman, S.T. Massie, D.P. Edwards, J.-M. Flaud, A. Perrin, C. Camy-Peyret, V. Danna, J.Y. Mandin, J. Schroeder, A. McCann, R.R. Gamache, R.B. Wattson, K. Yoshino, K.V. Chance, K.W. Jucks, L.R. Brown, V. Nemtchinov, P. Varanasi, J. Quantum Spectrosc. Radiat. Transf. **60**, 665 (1998)
31 L.S. Rothman, A. Barbe, D.C. Bennef, L.R. Brown, C. Camy-Peyret, M.R. Carleer, K. Chance, C. Clerbaux, V. Dana, V.M. Devi, A. Fayt, J.-M. Flaud, R.R. Gamache, A. Goldman, D. Jacquemart, K.W. Jucks, W.J. Lafferty, J.-Y. Mandin, S.T. Massie, V. Nemtchinov, D.A. Newnham, A. Perrin, C.P. Rinsland, J. Schroeder, K.M. Smith, M.A.H. Smith, K. Tang, R.A. Toth, J. Vander Auwera, P. Varanasi, K. Yoshino, J. Quantum Spectrosc. Radiat. Transf. **82**, 5 (2003)
32 L.S. Rothman, D. Jacquemart, A. Barbe, D.C. Benner, M. Birk, L.R. Brown, M.R. Carleer, C. Chackerian Jr, K. Chance, L.H. Coudert, V. Dana, V.M. Devi, J.-M. Flaud, R.R. Gamache, A. Goldman, J.-M. Hartmann, K.W. Jucks, A.G. Maki, J.-Y. Mandin, S.T. Massie, J. Orphal, A. Perrin, C.P. Rinsland, M.A.H. Smith, J. Tennyson, R.N. Tolchenov, R.A. Toth, J. Vander Auwera, P. Varanasi, G. Wagner, J. Quantum Spectrosc. Radiat. Transf. **96**, 139 (2005)
33 A. Wolf, *Aufbau eines Diodenlaser-basierten UV-Absorptionssensors für Stickstoffmonoxid* (Institute for Applied Physics, TU Darmstadt, Darmstadt, Germany, June 2003)
34 D.B. Fogel, IEEE Trans. Neural Netw. **5**, 3 (1994)
35 W.H. Press, S.A. Teukolsky, W.T. Vetterling, B.P. Flannery, *Numerical Recipes in FORTRAN 77: The Art of Scientific Computing, Vol. 1 of FORTRAN Numerical Recipes* (Cambridge University Press, Cambridge, 2001)
36 W.H. Press, S.A. Teukolsky, W.T. Vetterling, B.P. Flannery, *Numerical Recipes in FORTRAN 90: The Art of Parallel Scientific Computing, Vol. 2 of FORTRAN Numerical Recipes* (Cambridge University Press, Cambridge, 2002)
37 R. Barron-Jimenez, T.N. Anderson, J.A. Caton, R.P. Lucht, T. Walther, S. Roy, M.S. Brown, J.R. Gord, AIAA Paper No. 03-0402 (2003)
38 J.M. Hartmann, L. Rosenmann, M.Y. Perrin, J. Taine, Appl. Opt. **27**, 3063 (1988)
39 A. Predoi-Cross, C. Luo, P.M. Sinclair, J.R. Drummond, A.D. May, J. Mol. Spectrosc. **198**, 291 (1999)
40 P.M. Sinclair, P. Duggan, R. Berman, A.D. May, J.R. Drummond, J. Mol. Spectrosc. **181**, 41 (1997)
41 J.P. Bouanich, J. Quantum Spectrosc. Radiat. Transf. **13**, 953 (1973)
42 P. Varanasi, J. Quantum Spectrosc. Radiat. Transf. **15**, 191 (1975)
43 T. Nakazawa, M. Tanaka, J. Quantum Spectrosc. Radiat. Transf. **28**, 409 (1982)
44 S.M. Shoenung, R.K. Hanson, Combust. Sci. Technol. **24**, 227 (1981)
45 Q.V. Nguyen, B.L. Edgar, R.W. Dibble, A. Gulati, Combust. Flame **100**, 395 (1995)
46 B. Rosier, P. Gicquel, D. Henry, A. Coppalle, Appl. Opt. **27**, 360 (1988)
47 R.R. Skaggs, J.H. Miller, Combust. Flame **100**, 430 (1995)
48 R.D. Hancock, K.E. Bertagnolli, R.P. Lucht, Combust. Flame **109**, 323 (1997)
49 J.A. Silver, Appl. Opt. **31**, 707 (1992)